RSC Advances

PAPER

View Article Online
View Journal | View Issue

Cite this: *RSC Adv.*, 2021, **11**, 12867

Small functionalized iron oxide nanoparticles for dual brain magnetic resonance imaging and fluorescence imaging†

Ruixue Wei,*[a] Yang Liu,[a] Jinhao Gao,[b] V. Wee Yong[c] and Mengzhou Xue*[a]

Received 10th December 2020
Accepted 28th March 2021

DOI: 10.1039/d0ra10392f

rsc.li/rsc-advances

The diagnosis of brain diseases is the first key step in effective treatment. *In vivo* imaging tracers that effectively cross the blood–brain barrier (BBB) and reach areas of brain dysregulation is one focus of accurate diagnosis. Here, our main objective was to develop an iron-based nanoparticle for dual brain magnetic resonance imaging (MRI) and fluorescence imaging studies. Small sized iron oxide nanoparticles (SIONs) were prepared by a solvothermal method. Angiopep-2 was covalently connected to the surface of SIONs to enhance penetration of the BBB. The photosensitizer (chlorin e6, Ce6) was modified on the surface of SIONs to enhance fluorescence imaging to corroborate MRI results. We found that the resultant SIONs@ANG/Ce6/PEG displayed good biocompatibility and excellent MRI and fluorescence detection. Moreover, dual-modal MR/fluorescence imaging demonstrated that SIONs@ANG/Ce6/PEG had high sensitivity and accuracy in imaging of mouse with brain tumors. This work provides a strategy to design dual-modal contrast agents for diagnosis of brain disease.

Introduction

Magnetic resonance imaging (MRI) has been widely used in the diagnosis of brain diseases due to its non-invasive charcteristics and high spatial resolution.[1–3] At present, 40% to 50% of MRI examinations have used contrast agents to improve sensitivity,[4,5] including in diagnosis of brain tumors. Iron-based nanoparticles play a vital role in the field of MRI because of their nontoxic and excellent biocompatible properties.[6–10] Nevertheless, the presence of the blood–brain barrier (BBB) limits the penetration of tracers, which poses a challenge to brain MRI. The BBB is constituted of brain capillary endothelial cells (ECs), extracellular matrix protein-rich basement membranes, pericytes, and the endfeet of astrocytes.[11,12] These and the tight junctions (TJs) of endothelial cells severely limit the paracellular diffusion of water-soluble agents. Thus, the BBB is a physiologic barrier that limits the passage of most molecules in order to protect the stability of the brain.[13,14] Similarly, the BBB limits the entry into the brain of many contrast agents that could improve the diagnosis and evaluation of brain diseases, including brain tumors.

The surface of iron oxide nanoparticles can be functionalized with various targeting ligands to pass through the BBB. In addition, iron oxide nanoparticles play a vital role in the field of brain MRI, due to their excellent magnetic properties and ideal biocompatibility.[7,15] Nanoparticles containing brain tumor targeting ligands such as cRGD peptides,[16] antibody to EGFRvIII,[17] transferrin,[18,19] and chlorotoxin (CTX)[20] can be targeted to glioma tumors that originate within the central nervous system.[21–24] The angiopep family of peptides can also cross the BBB *via* a low-density lipoprotein receptor-related protein (LRP) mediated pathway.[13,25] Among them, angiopep-2 with a molecular weight of 2.4 kDa promotes receptor-mediated transport through LRP1, resulting in higher *in vivo* and *in vitro* transcytosis capacity than other targeting ligands.[26,27] Angiopep-2 can also target gliomas due to the high expression of LPR1 on the surface of glioma cells. Therefore, angiopep-2 has dual targeting capabilities of traversing the BBB and labeling gliomas, and this has generated great interest of in their potential use.

To improve upon nanoparticle-based delivery into the brain, several strategies for the diagnosis and treatment of brain tumors have been employed.[28–31] For instance, the median overall survival time of O6-benzylguanine (BG) modified superparamagnetic iron oxide nanoparticles was extended 3 times over that of the control group.[20] Besides, magnetic nanoparticles modified with polyethyleneimine (PEI) were constructed for drug delivery or gene loading and the

[a]*Department of Cerebrovascular Diseases, The Second Affiliated Hospital of Zhengzhou University, 2 Jingba Road, Zhengzhou 450052, Henan, 450001, China. E-mail: xuemengzhou@zzu.edu.cn*

[b]*State Key Laboratory of Physical Chemistry of Solid Surfaces, The MOE Laboratory of Spectrochemical Analysis & Instrumentation, The Key Laboratory for Chemical Biology of Fujian Province, College of Chemistry and Chemical Engineering, Xiamen University, Xiamen 361005, China*

[c]*Hotchkiss Brain Institute and Department of Clinical Neurosciences, University of Calgary, Calgary, Alberta, Canada*

† Electronic supplementary information (ESI) available: Hydrodynamic diameter and zeta potential of SIONs@NH_2 and SIONs@ANG/Ce6/PEG; fluorescence spectrum and UV-vis spectra of SIONs@ANG/Ce6/PEG. See DOI: 10.1039/d0ra10392f

accumulation in tumor sites by carotid injection was 30 times higher than that of intravenous injection.[32] The transferrin modified gold nanoparticles prepared by Davis *et al.* can promote the transport of nanoparticles across the BBB.[18] The Kataoka and his co-workers constructed a self-assembled supramolecular nanocarrier with glucose on its surface.[33] This system can target glucose transporter 1, which is highly expressed on brain capillary endothelial cells, and therefore allowing more accumulation in the brain. These studies have demonstrated that nanoparticles coated with targeting ligand can effectively improve the ability of nanoparticles to across the BBB.

Herein, we sought to improve iron-based nanoparticle for brain MR imaging. First, we synthesized small sized iron oxide nanoparticles (SIONs) by solvothermal method. The SIONs serve as T_1–T_2 dual modal MR contrast agents at low field. In addition, we modified SIONs by BBB targeting ligand and photosensitizer, angiopep-2 and chlorin e6 (Ce6), respectively, and incorporated PEG. Our results show that SIONs@ANG/Ce6/PEG achieves dual-modal imaging suitable for detection and imaging of experimental mice brain tumors.

Results and discussion

Synthesis and characterization of SIONs@ANG/Ce6/PEG

The procedure of synthesizing SIONs@ANG/Ce6/PEG is illustrated in Fig. 1a. Firstly, the SIONs were prepared according to a previously reported solvothermal method.[34,35] Subsequently, alendronate sodium was used to modify the SIONs to improve their solubility in water (SIONs@NH_2). Lastly, carboxyl-terminated PEG (mPEG2000–COOH), angiopep-2, and chlorin e6 (Ce6) were conjugated to the surface of SIONs@NH_2, yielding SIONs@ANG/Ce6/PEG.

The transmission electron microscope (TEM) image of SIONs revealed their spherical morphology and narrow size distribution (about 4.5 nm in diameter, Fig. 2a). The high-resolution TEM (HRTEM) image revealed that the lattice spacing distance of approximately 0.30 nm and 0.25 nm could be indexed to the {220} and {311} plane of magnetite, respectively (the inset of Fig. 2a). Dynamic light scattering (DLS) analysis showed that the hydrodynamic diameters (HDs) of SIONs@NH_2 and SIONs@ANG/Ce6/PEG were about 5.6 nm and 24.3 nm, respectively (Fig. S-1a† in the ESM and Table 1). The zeta potential of SIONs@ANG/Ce6/PEG (−25.7 mV) was slightly higher than that of SIONs@NH_2 (−32.8 mV) (Fig. S-1b and c† in the ESM and Table 1), which may be due to the contribution of PEG. The stability of nanomaterials is important for their biomedical applications. We then investigated the stability of SIONs@ANG/Ce6/PEG in serum solution (Fig. S-2 in the ESI†). The HDs of SIONs@ANG/Ce6/PEG were almost unchanged before and after incubated with 10% (v/v) fetal bovine serum (FBS) solution. The result suggested the good stability in FBS solution. The X-ray diffraction (XRD) patterns indicated the typical magnetite structure (JCPDS no. 65-3107, Fig. 2b).

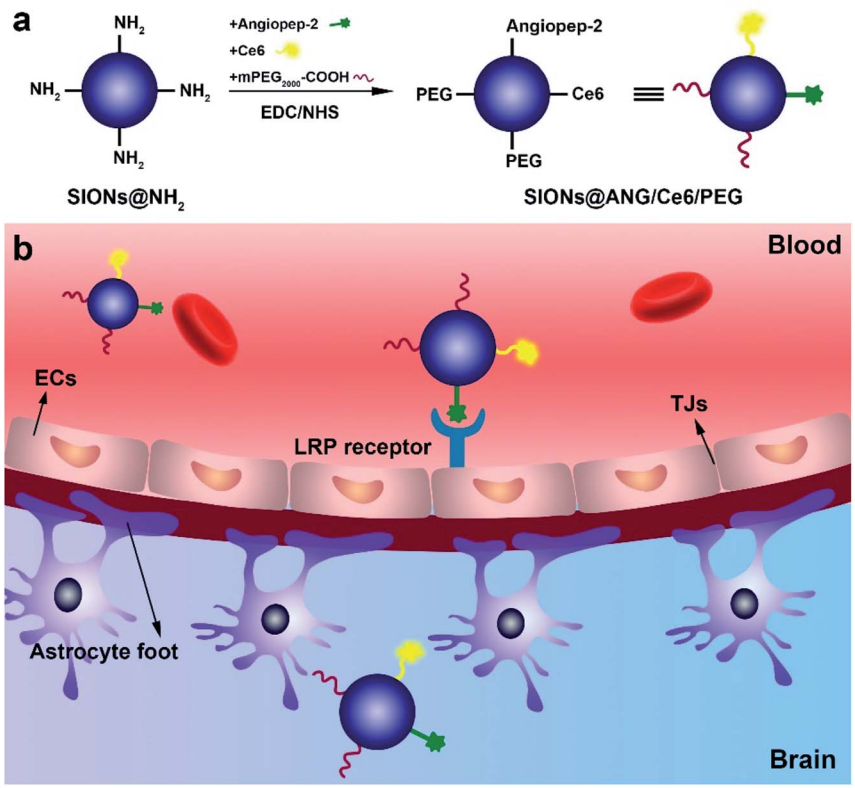

Fig. 1 (a) Schematic illustration of the synthesis of SIONs@ANG/Ce6/PEG. (b) Schematic of SIONs@ANG/Ce6/PEG transport across the blood–brain barrier (BBB) due to LRP1 receptor mediated transcytosis.

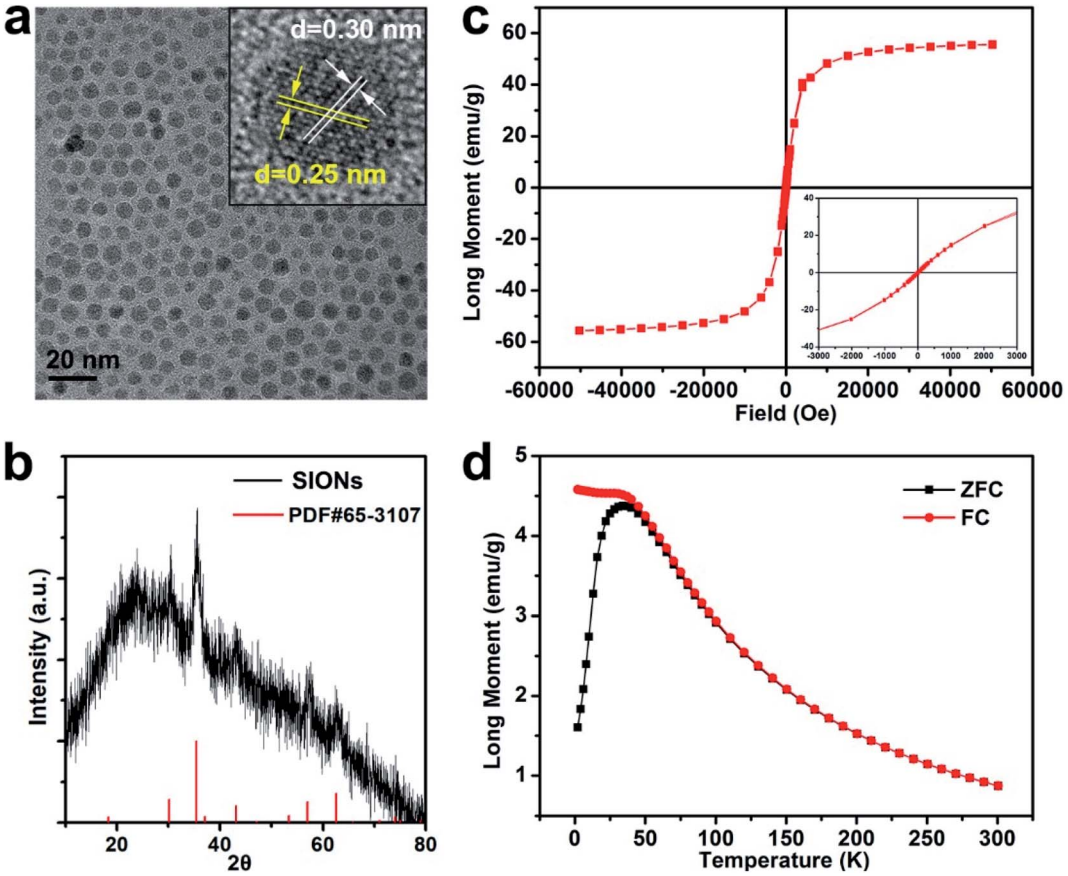

Fig. 2 Characterization of SIONs. (a) Transmission electron microscopy (TEM) image and high-resolution TEM image (inset) of SIONs. (b) X-ray powder diffraction (XRD) of SIONs. (c) Field-dependent magnetization curves (*M*–*H*) of SIONs at a magnetic field of 5 T at 300 K (insets: magnification of *M*–*H* curves from −3000 to 3000 Oe). (d) Zero field cooling and field cooling curves of SIONs. The ZFC–FC results show the blocking temperature is around 50 K.

Table 1 The hydrodynamic diameter and surface zeta potential of water-dispersible SIONs after coating in dynamic light scattering (DLS) analysis

Sample	HD/nm	PDI	Zeta potential/mV
SIONs@NH_2	5.6 ± 2.5	0.339	−32.8
SIONs@ANG/Ce6/PEG	24.3 ± 1.7	0.217	−25.7

We also used UV-vis spectrometry and fluorescence spectrum to assess the changes after modification by angiopep-2 and Ce6 (Fig. S-3 in the ESM†). The UV-vis results suggested that angiopep-2 and Ce6 were successfully coordinated on the surface of SIONs. The fluorescence spectrum of SIONs@ANG/Ce6/PEG further indicated the successful anchoring of Ce6 on the surface of SIONs (Fig. S-5 in the ESM†). The modification of SIONs surface was further confirmed by Fourier transform infrared (FT-IR) spectroscopy (Fig. S-6 in ESI†). The peak of 592 cm^{-1} was attributed to the vibration of Fe–O. The peaks of 2850 cm^{-1} and 2920 cm^{-1} belong to stretching vibration of saturated C–H, which supported the presence of $C_{17}H_{31}COO$– coated on the surface of SIONs. For SIONs@NH_2, the strong tightening of P=O and P–O vibration bands around 1044 cm^{-1} and 1144 cm^{-1}, which is characteristic of the chelation of phosphorus species on a metallic surface, indicating a coordination of phosphonates as chelating groups. The peak of 1631 cm^{-1} was affiliate to the bending vibration bands of –NH_2. In addition, the stretching vibration of saturated C–H disappeared. These results indicated that alendronate was successfully grafted onto the surface of SIONs through the phosphonate groups. For SIONs@ANG/Ce6/PEG, the absorption band at 1642 cm^{-1} attributed to stretching vibration of –NH. In contrast to the spectrum of SIONs@NH_2, the stretching vibration of saturated C–H reappeared, which indicated the conjugation of PEG. The peaks at 3404 cm^{-1} and 1384 cm^{-1} showed conjugation of Ce6. These results suggested that the successful functionalization of SIONs by angiopep-2, Ce6, and PEG. Next, we used UV-vis spectrometry to evaluate the amount of angiopep-2 and Ce6 loaded on the surface of SIONs@NH_2. After subtracting the absorption background of SIONs@NH_2, the loading capacity was evaluated by calibration curve of free Ce6 (Fig. S-4 in the ESI†). The loading capacity of angiopep-2 was estimated by subtracting the unloaded dose from the total dose. Each magnetite nanoparticle could load about 37 angiopep-2 molecules and 52 Ce6 molecules.

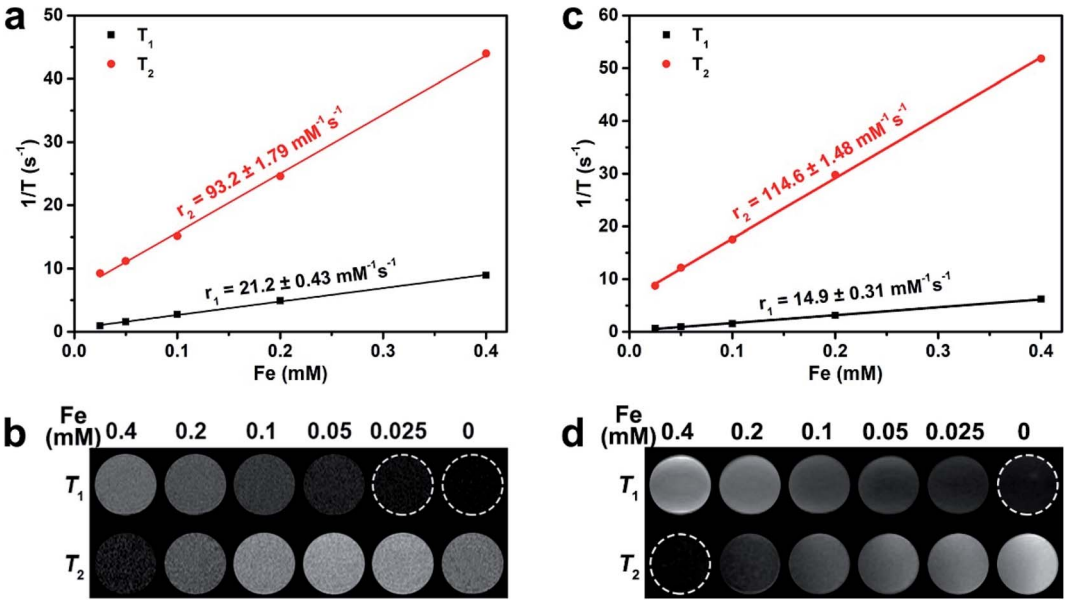

Fig. 3 Relaxivity measurements of SIONs. T_1 relaxation rate ($1/T_1$) and T_2 relaxation rate ($1/T_2$) plotted as a function of c_{Fe} for SIONs at (a) 0.5 T and (b) 1.5 T. T_1-/T_2-weighted phantom imaging of SIONs acquired on a (c) 0.5 T scanner and (d) 1.5 T.

Magnetic properties and relaxivity measurements of SIONs

Magnetic behavior of SIONs was measured at a magnetic field of 5 T by using a superconducting quantum interference device (SQUID) at 300 K. The magnetic saturation moments (M_S) value of SIONs was 55.3 emu g^{-1} (Fig. 2c). The field-dependent magnetization curves (M–H) indicated that SIONs exhibit typical superparamagnetic behavior at 300 K (Fig. 2c, and inset). Additionally, standard zero-field cooling (ZFC) and field cooling (FC) measurements for SIONs showed a blocking temperature (T_B) of about 50 K, which suggests superparamagnetic characteristics of SIONs at room temperature (Fig. 2d).

To evaluate the MR contrast ability of SIONs, the longitudinal relaxivity (r_1) and transverse relaxivity (r_2) values were measured on a 0.5 T MRI scanner (Fig. 3a and Table 2). The r_1 and r_2 values as a function of c_{Fe} for SIONs were 21.2 ± 0.43 mM^{-1} s^{-1} and 93.2 ± 1.79 mM^{-1} s^{-1}, respectively. r_2/r_1 ratio is a key reference to predict whether a contrast agent is suitable for T_1- or T_2-dominated MR imaging.[36,37] Generally, a high r_2/r_1 ratio (>10) will result in a T_2 performance dominance, while a low r_2/r_1 ratio (<5) will result in a T_1 performance dominance.[3,38] The r_2/r_1 ratio of SIONs was 4.4, indicating that SIONs can serve as a T_1–T_2 dual-modal contrast agent. SIONs showed increased signals in T_1-weighted phantom images and reduced signals in T_2-weighted phantom images at 0.5 T with increased iron concentrations (Fig. 3b and Table 2). We also measured the relaxation performance of SIONs at 1.5 T (Fig. 3c and d), because the relaxation efficiency of magnetic nanomaterials is closely related to the magnetic field strength. The r_1 and r_2 value were 14.9 ± 0.31 mM^{-1} s^{-1} and 114.6 ± 1.48 mM^{-1} s^{-1}, respectively. The r_2/r_1 ratio was 7.9, which was higher than the result at 0.5 T. These phenomena further indicated that SIONs may possess the T_1–T_2 dual-modal MR contrast ability at low magnetic field.

Table 2 The T_1 and T_2 relaxivities (at 0.5 and 1.5 T) of SIONs measured at 300 K

Magnetic field	Relaxivity	
0.5 T	r_2 (mM^{-1} s^{-1})	93.2 ± 1.79
	r_1 (mM^{-1} s^{-1})	21.2 ± 0.43
	r_2/r_1	4.4
1.5 T	r_2 (mM^{-1} s^{-1})	114.6 ± 1.48
	r_1 (mM^{-1} s^{-1})	14.9 ± 0.31
	r_2/r_1	7.9

According to SBM theory, longitudinal relaxation is closely related to the direct chemical exchange between water protons and surface paramagnetic ions.[39,40] Small-sized nanoparticles have higher surface-area-to-volume ratios than large-sized nanoparticles and then exposed more iron ions, which enhances the chemical exchange and improves their performance in shortening the spin-lattice relaxation. Therefore, small-sized iron-based nanoparticles were more likely to exhibit T_1 performance than large-sized nanoparticles due to more paramagnetic ions on the surface. r_2 relaxivity of contrast agent can be calculated by using the following formula:[41,42]

$$\frac{1}{T_2}\frac{\left(\frac{256\pi^2\gamma^2}{405}\right)V^*{M_S}^2r^2}{D\left(1+\frac{L}{r}\right)}$$

(γ: the magnetic ratio constant, D: the diffusion constant of water protons, L: the thickness of an impermeable surface of magnetic nanoparticles, V^*: the effective volume fraction, M_S: the saturation magnetization, and r: the effective radius). Generally, γ, D and L are constant. V^* is related to the concentration of contrast agent and is also constant in practice. The T_2 relaxation performance of the contrast agent mainly depends on M_S and r. Therefore, the

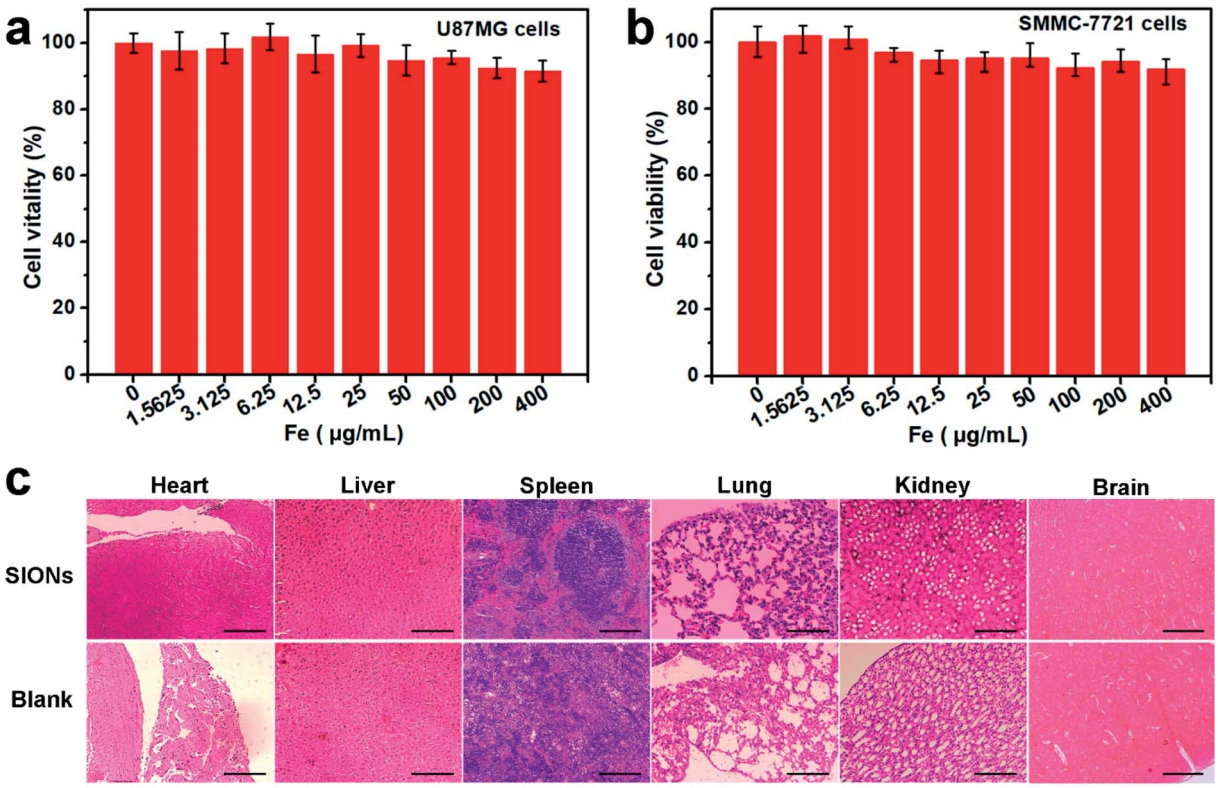

Fig. 4 Biocompatibility of SIONs. Cell viability of (a) U87MG cells and (b) SMMC-7721 cells treated with SIONs for 24 h. $n = 5$ per group. (c) H&E stained tissue sections from nude mice collected at 4 days after injection of SIONs or PBS (blank). Scale bar for all images: 200 μm.

surface paramagnetic ions and the suitable M_S values of SIONs indicated that SIONs may have the T_1–T_2 dual-modal MR contrast capability under a low magnetic field.

Biocompatibility of SIONs

Next, we focused on the biocompatibility of SIONs. The cell cytotoxicity was evaluated with U87MG cells and SMMC-7721 cells by tetrazolium-based colorimetric (MTT) assays (Fig. 4a and b). After 24 h of incubation, cell viability exceeded 90% even at 400 μg [Fe] mL^{-1}. The toxicity of SIONs *in vivo* was further investigated by histological analysis. After intravenous injection of SIONs at a dose of 20 mg Fe per kg, we collected several organs of nude mice for hematoxylin and eosin (H&E) staining (Fig. 4c). There were no apparent cell necrosis and apoptosis in the sections of organs. To further evaluate red blood cells compatibility under SIONs administration, a standard hemolysis assay was performed as Fig. S-7† in the ESM. The diluted red blood cells were exposed to SIONs at a concentration gradient and no significant hemolysis effect were observed at even 3.6 mM [Fe] till 4 h incubation, which demonstrated ideal blood stability of the SIONs. These results suggest that SIONs exhibit excellent biocompatibility which permit their further biological application.

In vivo fluorescence and MR imaging

We further investigated the ability of SIONs@ANG/Ce6/PEG to cross the BBB into brain. Considering the fluorescent property of Ce6, we performed *in vivo* fluorescence imaging (Fig. 5) of nude mice after intravenous injection of the SIONs@ANG/Ce6/PEG or free Ce6 at the same dose of 2 mg Ce6 per kg body weight, respectively. All animal procedures were performed in accordance with the Guidelines for Care and Use of Laboratory Animals of Zhengzhou University and approved by the Animal Ethics Committee of The Second Affiliated Hospital of Zhengzhou University. After 1.5 h post injection, the increased fluorescence signal of brain indicates that SIONs@ANG/Ce6/PEG can successfully cross BBB. In contrast, the mice injected with free Ce6 showed scarcely visible fluorescence signals in brain, because of the inability of free Ce6 to cross the BBB.

To assess the T_1/T_2 contrast performance of SIONs@ANG/Ce6/PEG, *in vivo* MR imaging of the brain of nude mice was performed on a 9.4 T MRI scanner. After tail vein injection of

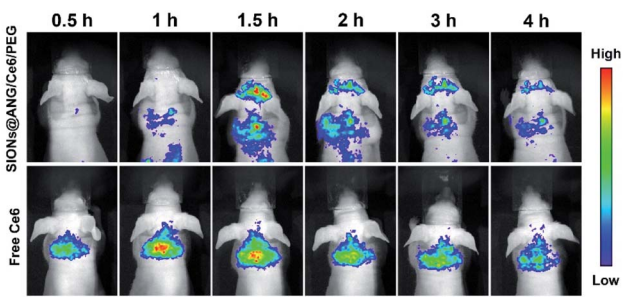

Fig. 5 *In vivo* fluorescence images of nude mice taken at different time points after intravenous injection of SIONs@ANG/Ce6/PEG or free Ce6 at the same dose of 2 mg Ce6 per kg body weight.

SIONs@ANG/Ce6/PEG, T_1-weighted and T_2-weighted images were acquired at different time points (Fig. 6a and b). Remarkable T_1 signals were observed in brain region at 2 h post injection, and the bright signal in brain lasted for about 4 h post injection. Fig. 5c showed the quantitative analysis of brain after injection of SIONs@ANG/Ce6/PEG. The SNR_{post}/SNR_{pre} increased after intravenous injection, and reached 1.45 ± 0.10, 1.48 ± 0.08, and 1.44 ± 0.04 at 2, 3, and 4 h post injection for the transverse plane, respectively. The SNR_{post}/SNR_{pre} values were 1.27 ± 0.09, 1.34 ± 0.05, and 1.12 ± 0.09 at 2, 3, and 4 h post injection for the coronal plane, respectively. T_2-weighted imaging also indicated dark signal in brain after 2 h post injection. The SNR_{post}/SNR_{pre} values at 2, 3, and 4 h after injection were 0.6551 ± 0.01, 0.67 ± 0.06, and 0.69 ± 0.06 for the transverse plane, and 0.46 ± 0.04, 0.49 ± 0.04, and 0.48 ± 0.03 for the coronal plane, respectively. The MRI manifested that SIONs@ANG/Ce6/PEG could cross the BBB and reach the brain region, which was consistent with the result of fluorescence imaging. Thus, SIONs@ANG/Ce6/PEG is a potential candidate for brain MR contrast agents.

In vivo biodistribution analysis

The biodistribution of nanoparticles are crucial in *in vivo* biomedical applications. We assessed the biodistribution of iron in nude mice after administration of SIONs@NH_2 and SIONs@ANG/Ce6/PEG, and measured by inductively coupled plasma mass spectromtry (ICP-MS). We observed higher iron accumulation in the brain after administration of SIONs@ANG/Ce6/PEG than that of SIONs@NH_2 (Fig. S-8† in the ESM). The biodistribution of iron further indicated that the targeting properties of the SIONs@ANG/Ce6/PEG due to the conjugation of angiopep-2.

Experimental section

Materials

All chemicals were purchased from various vendors and used as received without further purification: alendronate sodium (98%), iron(II) chloride tetrahydrate (98%), and chlorin e6 (Ce6) were purchased from Sigma-Aldrich. Oleic acid (tech 90%) were purchased from Alfa Aesar. Ammonium iron(II) sulfate and ethyl alcohol were purchased from Sinopharm Chemical Reagent. mPEG–COOH (M_W = 2000) was purchased from Biomatrik (China). 1-(3-Dimethylaminopropyl)-3-ethylcarbodiimide hydrochloride (EDC) and *N*-hydroxysuccinimide (NHS) were purchased from Thermo Fisher Scientific.

Characterization

Transmission electron microscopy (TEM) and high-resolution TEM (HRTEM) images were captured on a JEM-2100 microscope at an accelerating voltage of 200 kV. Element analysis of Fe in the samples were conducted by inductively coupled plasma atomic emission spectroscopy (ICP-AES). X-ray powder diffraction (XRD) patterns were obtained on a Rigaku UltimaIV X-ray diffractometer, equipped with a Cu Kα radiation source (λ = 0.15418 nm). Field-dependent magnetization curves (*M–H* curves) were obtained *via* a superconducting quantum interference device (SQUID). Hydrodynamic diameters of nanoparticles were measured *via* dynamic light scattering (DLS) on a Malvern Zetasizer nano ZS instrument. MRI measurements and T_1/T_2 relaxation time measurements were carried out on

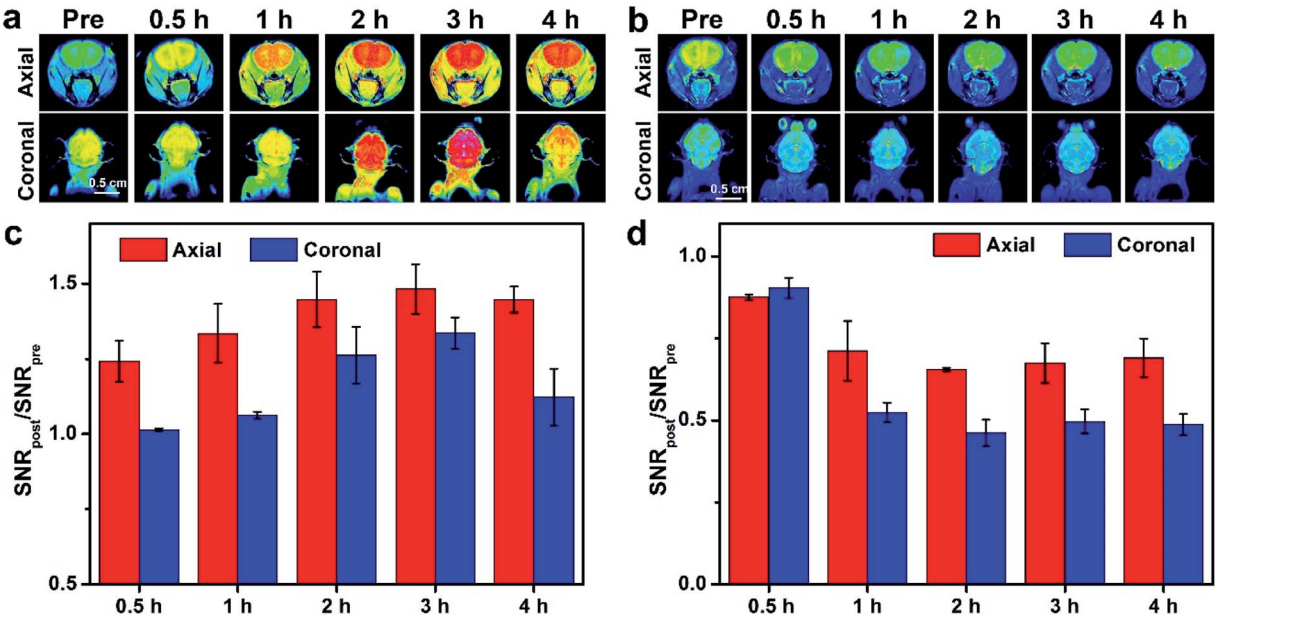

Fig. 6 *In vivo* MR imaging at 9.4 T. *In vivo* (a) T_1-weighted and (b) T_2-weighted MR imaging of nude mice before and after intravenous injection of SIONs@ANG/Ce6/PEG at a dose of 2 mg Fe per kg body weight. (c) and (d) Quantification of signal-to noise ratio changes (SNR) in the brain after intravenous injection of SIONs@ANG/Ce6/PEG at different time points (n = 3 per group) in (a) and (b), respectively.

a 20 MHz NMR120-Analyst NMT Analyzing&Imaging system (Niumag Corporation, Shanghai). *In vivo* MR images were obtained on a 9.4 T MRI scanner system (Philips Medical System).

Synthesis of small sized iron oxide nanoparticles (SIONs)

The synthesis of iron oxide nanoparticles was carried out according to a modification of solvothermal method. In a typical synthesis, 1 g of NaOH, 10 mL of H_2O, 10 mL of ethanol, and 10 mL of oleic acid (OA) were mixed together to form a uniform microemulsion. 10 mL 0.5 M of $FeCl_2 \cdot 4H_2O$ aqueous solution was then added after stirring for 0.5 h. The resulting solution was stirred for 2 min before transfer into an autoclave and kept at 170 °C for 10 h. After the system cooled to room temperature, ethanol was added to precipitate iron oxide nanoparticles. The black product was then washed three times with ethanol and well-dispersed in hexane.

Preparation of NH_2 modified SIONs

Forty milligram of alendronate sodium was dissolved in 4 mL of deionized water, and the pH was adjusted to 7.5. Four mL of acetone was then added followed by 2 mL of *n*-hexane containing 10 mg of IO nanoparticles. The resulting solution was heated to 60 °C under a N_2 atmosphere for 2 h. The NH_2 modified IO nanoparticles were obtained by centrifugation, re-dispersed in deionized water, and stored at 4 °C. The product was abbreviated as SIONs@NH_2.

Preparation of SIONs@ANG/Ce6/PEG

Ten mg of EDC and 10 mg NHS were dissolved in 4 mL of DMSO; 1 mg angiopep-2, 1 mg of Ce6, 5 mg of $mPEG_{2000}$–COOH were added after dissolution. The resulting solution was stirred for 1 h at room temperature to activate the carboxyl group. Then, 4 mL of deionized water containing 10 mg of SIONs@NH_2 was added. After stirring for 24 h, SIONs@ANG/Ce6/PEG was collected by ultrafiltration, re-dispersed in PBS (1×, pH 7.4), and stored at 4 °C.

Relaxivity measurement and MRI phantom studies of SIONs@NH_2

T_1 and T_2 relaxation time and T_1/T_2-wighted phantom images of SIONs@NH_2 were acquired on a 0.5 T NMI20-Analyst NMR Analyzing and Imaging system. The samples were dispersed in PBS (1×, pH 7.4) with different Fe concentrations at 0.4, 0.2, 0.1, 0.05, 0.025 mM. The r_1 and r_2 were calculated from the slopes of the best fitted lines of $1/T$ *versus* iron. The T_1-/T_2-weighted phantom images were acquired with the following parameters: TR/TE = 200/2 ms (T_1), TR/TE = 2000/40 ms (T_2), NS = 2.

In vitro cytotoxicity assay

U87MG cells were purchased from the Cell Bank of the Chinese Academy of Sciences (Shanghai, China). Cytotoxicity was assessed *via* 3-(4,5-dimethylthiazol-2-yl)-2,5-diphenyltetrazolium bromide (MTT) assay. Typically, U87MG cells ($n = 5$ per group) were seeded into 96-well plates at 5×10^3 cells per well and incubated for 24 h. The cells were then incubated with SIONs@NH_2 for 24 h at different concentrations (0, 1.5625, 3.125, 6.25, 12.5, 25, 50, 100, 200 and 400 μg mL^{-1} for Fe). After the medium of each well was replaced by 100 μL of fresh media containing MTT (0.5 mg mL^{-1}), the cells were incubated for 4 h. Finally, the medium was removed and 100 μL of DMSO was added to completely dissolve the resulting violet crystals. The absorbance of each well at 492 nm was measured on a Multiskan FC microplate reader. The cell viability at different concentrations was calculated accordingly.

In vivo fluorescence imaging study

All animal procedures were performed in accordance with the Guidelines for Care and Use of Laboratory Animals of Zhengzhou University and approved by the Animal Ethics Committee of The Second Affiliated Hospital of Zhengzhou University. *In vivo* fluorescence imaging was carried out on an IVIS Lumina II. Nude male mice (18–22 g) were intravenously injected with SIONs@ANG/Ce6/PEG and free Ce6 at a dose of 2 mg Ce6 per kg. The mice were imaged by fluorescence imaging system before and at 0.5, 1, 1.5, 2, 3, and 4 h post injection.

In vivo MRI study

All animal procedures were performed in accordance with the Guidelines for Care and Use of Laboratory Animals of Zhengzhou University and approved by the Animal Ethics Committee of The Second Affiliated Hospital of Zhengzhou University. MR imaging was performed on a 9.4 T MRI scanner. Male nude mice (body weight: 18–22 g) were used for *in vivo* MR imaging ($n = 3$ per group). SIONs@ANG/Ce6/PEG were injected intravenously *via* the tail vein into nude mice at a dose of 2 mg iron per kg. The T_1-/T_2-weighted MR images were acquired at different times after administration using FSEMS and FSE sequence, respectively. The parameters were as follows: TR/TE (T_1) = 500/14 ms, TR/TE (T_2) = 3000/4 ms, thickness = 1.5 mm, data matrix (RO × PE) = 256 × 256. SNR was calculated by the following equation:

$$SNR_{brain} = SI_{brain}/SD_{noises}$$

Biodistribution study

Male nude mice (body weight: 18–22 g) were utilized for performing the biodistribution of SIONs and SIONs@ANG/Ce6/PEG. SIONs and SIONs@ANG/Ce6/PEG were tail vein intravenously injected into mice at dose of 20 mg iron per kg ($n = 3$ per group). 20 mg of brain, heart, liver, spleen, lung, and kidney were collected at 2 h after injection for biodistribution using inductively coupled plasma mass spectromtry (ICP-MS).

Conclusions

In conclusion, we developed iron-based nanoparticles for brain dual-modal MR and fluorescence imaging. Uniform and monodisperse SIONs were synthesized by solvothermal method. Relaxivity measurements and *in vitro* phantom imaging demonstrate the excellent T_1 and T_2 contrast

performance of SIONs at low magnetic field, which is attributed to the suitable magnetization and surface paramagnetic ions of SIONs. More importantly, the outstanding biocompatibility of SIONs@ANG/Ce6/PEG allows its further biological application. After modification by BBB targeted peptide angiopep-2, SIONs@ANG/Ce6/PEG transports across the *in vivo* BBB of nude mice. SIONs@ANG/Ce6/PEG can be used for *in vivo* fluorescence due to the conjugation of Ce6. The targeting performance of SIONs@ANG/Ce6/PEG was manifested by *in vivo* fluorescence and MR imaging. In summary, we believe that SIONs@ANG/Ce6/PEG hold great potential in brain MR imaging.

Conflicts of interest

There are no conflicts to declare.

Acknowledgements

The authors acknowledge operating grant support from the National Natural Science Foundation of China (81870942, 81471174 and 81520108011), National Key Research and Development Program of China (2018YFC1312200), Funded by China Postdoctoral Science Foundation (2020TQ0289), and Innovation Scientists and Technicians Troop Constructions Projects of Henan Province of China (for MX).

Notes and references

1 R. Wei, Z. Cai, B. W. Ren, A. Li, H. Lin, K. Zhang, H. Chen, H. Shan, H. Ai and J. Gao, *Chem. Mater.*, 2018, **30**, 7950–7961.
2 W. Liu, G. Deng, D. Wang, M. Chen, Z. Zhou, H. Yang and S. Yang, *J. Mater. Chem. B*, 2020, **8**, 3087–3091.
3 R. Wei, T. Zhou, C. Sun, H. Lin, L. Yang, B. W. Ren, Z. Chen and J. Gao, *Nanoscale*, 2018, **10**, 18398–18406.
4 J. H. Lee, Y. M. Huh, Y. W. Jun, J. W. Seo, J. T. Jang, H. T. Song, S. Kim, E. J. Cho, H. G. Yoon, J. S. Suh and J. Cheon, *Nat. Med.*, 2007, **13**, 95–99.
5 M. C. Cassidy, H. R. Chan, B. D. Ross, P. K. Bhattacharya and C. M. Marcus, *Nat. Nanotechnol.*, 2013, **8**, 363–368.
6 B. Zhou, H. Shan, D. Li, Z. B. Jiang, J. S. Qian, K. S. Zhu, M. S. Huang and X. C. Meng, *Magn. Reson. Imag.*, 2010, **28**, 394–399.
7 L. Yang, Z. Zhou, J. Song and X. Chen, *Chem. Soc. Rev.*, 2019, **48**, 5140–5176.
8 C. Jiang, G. Wang, R. Hein, N. Liu, X. Luo and J. J. Davis, *Chem. Rev.*, 2020, **120**, 3852–3889.
9 D. Anderson, T. Anderson and F. Fahmi, *Phys. Status Solidi A*, 2019, **216**, 1801008.
10 H. Fatima and K.-S. Kim, *Adv. Powder Technol.*, 2018, **29**, 2678–2685.
11 W. Tang, W. Fan, J. Lau, L. Deng, Z. Shen and X. Chen, *Chem. Soc. Rev.*, 2019, **48**, 2967–3014.
12 J. B. Xie, Z. Y. Shen, Y. Anraku, K. Kataoka and X. Y. Chen, *Biomaterials*, 2019, **224**, 119491.
13 X. X. Shi, W. M. Miao, D. W. Pang, J. S. Wu, Q. S. Tong, J. X. Li, J. Q. Luo, W. Y. Li, J. Z. Du and J. Wang, *Biomater. Sci.*, 2020, **8**, 1290–1297.
14 W. M. Pardridge, *Drug Discov. Today*, 2001, **6**, 381–383.
15 R. Wei, Y. Xu and M. Xue, *J. Mater. Chem. B*, 2021, **9**, 1965–1979.
16 S. Richard, M. Boucher, Y. Lalatonne, S. Meriaux and L. Motte, *Biochim. Biophys. Acta Gen. Subj.*, 2017, **1861**, 1515–1520.
17 C. G. Hadjipanayis, R. Machaidze, M. Kaluzova, L. Wang, A. J. Schuette, H. Chen, X. Wu and H. Mao, *Cancer Res.*, 2010, **70**, 6303–6312.
18 A. J. Clark and M. E. Davis, *Proc. Natl. Acad. Sci. U. S. A.*, 2015, **112**, 12486–12491.
19 S. Ruan, L. Qin, W. Xiao, C. Hu, Y. Zhou, R. Wang, X. Sun, W. Yu, Q. He and H. Gao, *Adv. Funct. Mater.*, 2018, **28**, 1802227.
20 Z. R. Stephen, F. M. Kievit, O. Veiseh, P. A. Chiarelli, C. Fang, K. Wang, S. J. Hatzinger, R. G. Ellenbogen, J. R. Silber and M. Zhang, *ACS Nano*, 2014, **8**, 10383–10395.
21 P. Zhao, Y. Wang, X. Kang, A. Wu, W. Yin, Y. Tang, J. Wang, M. Zhang, Y. Duan and Y. Huang, *Chem. Sci.*, 2018, **9**, 2674–2689.
22 D. Furtado, M. Bjornmalm, S. Ayton, A. I. Bush, K. Kempe and F. Caruso, *Adv. Mater.*, 2018, **30**, 1801362.
23 S. M. Carvalho, A. G. Leonel, A. A. P. Mansur, I. C. Carvalho, K. Krambrock and H. S. Mansur, *Biomater. Sci.*, 2019, **7**, 2102–2122.
24 Y. Yin, J. Wang, M. Yang, R. Du, G. Pontrelli, S. McGinty, G. Wang, T. Yin and Y. Wang, *Nanoscale*, 2020, **12**, 2946–2960.
25 H. Xin, X. Sha, X. Jiang, L. Chen, K. Law, J. Gu, Y. Chen, X. Wang and X. Fang, *Biomaterials*, 2012, **33**, 1673–1681.
26 K. Shao, R. Huang, J. Li, L. Han, L. Ye, J. Lou and C. Jiang, *J. Contr. Release*, 2010, **147**, 118–126.
27 M. Demeule, J.-C. Currie, Y. Bertrand, C. Che, T. Nguyen, A. Regina, R. Gabathuler, J.-P. Castaigne and R. Beliveau, *J. Neurochem.*, 2008, **106**, 1534–1544.
28 J. Xie, D. Gonzalez-Carter, T. A. Tockary, N. Nakamura, Y. Xue, M. Nakakido, H. Akiba, A. Dirisala, X. Liu, K. Toh, T. Yang, Z. Wang, S. Fukushima, J. Li, S. Quader, K. Tsumoto, T. Yokota, Y. Anraku and K. Kataoka, *ACS Nano*, 2020, **14**, 6729–6742.
29 H. S. Min, H. J. Kim, M. Naito, S. Ogura, K. Toh, K. Hayashi, B. S. Kim, S. Fukushima, Y. Anraku, K. Miyata and K. Kataoka, *Angew. Chem., Int. Ed.*, 2020, **59**, 8173–8180.
30 Y. Wang, K. Wang, J. Zhao, X. Liu, J. Bu, X. Yan and R. Huang, *J. Am. Chem. Soc.*, 2013, **135**, 4799–4804.
31 I. U. Ali and X. Chen, *ACS Nano*, 2015, **9**, 9470–9474.
32 B. Chertok, A. E. David and V. C. Yang, *Biomaterials*, 2010, **31**, 6317–6324.
33 Y. Anraku, H. Kuwahara, Y. Fukusato, A. Mizoguchi, T. Ishii, K. Nitta, Y. Matsumoto, K. Toh, K. Miyata, S. Uchida, K. Nishina, K. Osada, K. Itaka, N. Nishiyama, H. Mizusawa, T. Yamasoba, T. Yokota and K. Kataoka, *Nat. Commun.*, 2017, **8**, 1001.

34 X. Wang, J. Zhuang, Q. Peng and Y. D. Li, *Nature*, 2005, **437**, 121–124.
35 C. Li, R. Wei, Y. Xu, A. Sun and L. Wei, *Nano Res.*, 2015, **7**, 536–543.
36 P. Caravan, J. J. Elliso, T. J. McMurry and R. B. Lauffer, *Chem. Rev.*, 1999, **99**, 2293–2352.
37 M. Lei, C. Fu, X. Cheng, B. Fu, N. Wu, Q. Zhang, A. Fu, J. Cheng, J. Gao and Z. Zhao, *Adv. Funct. Mater.*, 2017, **27**, 1700978.
38 L. Yang, L. Ma, J. Xin, A. Li, C. Sun, R. Wei, B. W. Ren, Z. Chen, H. Lin and J. Gao, *Chem. Mater.*, 2017, **29**, 3038–3047.
39 I. Solomon, *Phys. Rev.*, 1955, **99**, 559–565.
40 N. Bloembergen and L. O. Morgan, *J. Chem. Phys.*, 1961, **34**, 842–850.
41 S. Tong, S. Hou, Z. Zheng, J. Zhou and G. Bao, *Nano Lett.*, 2010, **10**, 4607–4613.
42 Z. Zhao, Z. Zhou, J. Bao, Z. Wang, J. Hu, X. Chi, K. Ni, R. Wang, X. Chen, Z. Chen and J. Gao, *Nat. Commun.*, 2013, **4**, 2266.